

Mamba2D: A Natively Multi-Dimensional State-Space Model for Vision Tasks

Enis Baty^{1*}, Alejandro Hernández Díaz^{1*}, Rebecca Davidson², Chris Bridges¹, and Simon Hadfield¹

¹ University of Surrey, Guildford, England

{e.baty, a.hernandez, c.p.bridges, s.hadfield}@surrey.ac.uk

² Surrey Satellite Technology Limited, Guildford, England
bdavidson@sstl.co.uk

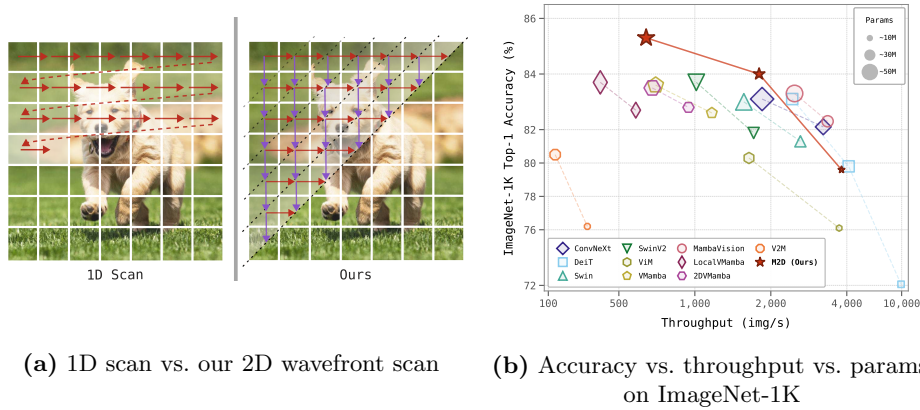


Fig. 1. (a) Comparison of traditional rasterised scanning (left) vs. our native 2D wavefront scan (right); diagonals indicate parallel computation steps. (b) M2D (stars) establishes a new accuracy-throughput-params frontier for SSM vision models.

Abstract. State-Space Models (SSMs) have emerged as an efficient alternative to transformers, yet existing visual SSMs retain deeply ingrained biases from their origins in natural language processing. In this paper, we address these limitations by introducing M2D-SSM, a ground-up re-derivation of selective state-space techniques for multidimensional data. Unlike prior works that apply 1D SSMs directly to images through arbitrary rasterised scanning, our M2D-SSM employs a single 2D scan that factors in both spatial dimensions natively. On ImageNet-1K classification, M2D-T achieves 84.0% top-1 accuracy with only 27M parameters, surpassing all prior SSM-based vision models at that size. M2D-S further achieves 85.3%, establishing state-of-the-art results among SSM-based architectures. Across downstream tasks, Mamba2D achieves 52.2 box AP on MS-COCO object detection (3× schedule) and 51.7 mIoU on ADE20K segmentation, demonstrating strong generalisation and efficiency at scale. Source code is available at <https://github.com/cocoalex00/Mamba2D>.

Keywords: State-Space Models · Vision Backbone · Image Classification · Object Detection · Semantic Segmentation

1 Introduction

Since the introduction of the Vision Transformer (ViT) [10], countless works have explored their use across a wide range of visual tasks [44,6,15,23,28,27,1], fundamentally reshaping how image data is processed and interpreted. However, transformer attention exhibits a well-documented quadratic scaling in complexity relative to image size. This behaviour leads to substantial computational overhead, becoming particularly problematic in high-resolution or dense tasks like detection, segmentation, remote sensing or medical imaging.

In response, recent work in language modelling has introduced State Space Models (SSMs) as a promising alternative, offering linear scaling in complexity with respect to input length. Mamba [12] advanced this further with a novel selectivity mechanism that dynamically aggregates global context in a manner analogous to attention.

However, SSM adoption in vision has highlighted inherent biases stemming from their language-model origins: (1) SSMs were proposed for 1-dimensional signals and cannot be applied to multidimensional data without reshaping; (2) the causal structure, suited to language, does not align with the predominantly non-causal requirements of vision.

These limitations have been partially addressed in previous works by applying unrolling strategies on 2D images, reshaping them into multiple 1D sequences that are scanned individually and fused to capture spatial relationships. Unfortunately, the recurrent memory of SSMs provides exponentially decaying recall with distance. This makes them sensitive to data locality, which no combination of 2D-to-1D mappings can faithfully preserve. In other words, neighbourhood relationships in the image space cannot be reliably mapped to the 1D SSM space.

In contrast, we fundamentally re-design the State-Space paradigm to produce the M2D-SSM: a natively 2D block that preserves the selectivity of Mamba while enabling information flow across both spatial dimensions concurrently, faithfully capturing 2D neighbourhood structure without 1D flattening. These 2D dependencies are incompatible with prior parallel scan approaches, requiring a custom CUDA wavefront-scan kernel (Section 3.3). We then exploit this to construct a hybrid architecture pairing M2D-SSM blocks with vanilla attention: M2D-SSM handles high-resolution stages where its linear scaling excels, while vanilla attention is applied at low-resolution stages, where spatial cost is minimal.

To the best of our knowledge, no prior work derives a native 2D SSM for vision without workarounds that sacrifice 2D spatial structure. Our primary contributions are: (1) A natively 2D SSM formulation that faithfully operates on both spatial dimensions without 1D flattening. (2) A custom fused CUDA wavefront-scan kernel enabling parallelisable training of the 2D recurrence, which we release publicly. (3) A hybrid architecture that synergistically combines M2D-SSMs at high resolution with vanilla attention at low resolution, without windowing or other capacity compromises. (4) State-of-the-art results among SSM-based models on ImageNet-1K classification, MS-COCO detection, and ADE20K segmentation.

2 Related Work

The Vision Transformer (ViT) [10] demonstrated that patch-based transformers can match or surpass CNNs on large-scale image classification, with DeiT [36] improving data efficiency via distillation. However, the quadratic cost of global self-attention limits scalability to high-resolution inputs. This motivated hierarchical variants such as Swin [28,27] and PVT [40], which use local windows or progressive spatial reduction. Modernised CNNs such as ConvNeXt [30] remain competitive, and various hybrid architectures have been proposed [6,15,23] to leverage the complementary strengths of both paradigms.

State-space models (SSMs) offer a compelling alternative for sequence modelling, driven by their linear scaling with sequence length. The foundational S4 model [14] established that SSMs could effectively model long-range dependencies by leveraging efficient parameterization and HiPPO initialization [13]. A critical breakthrough came with Mamba [12], which introduced an input-dependent selective scan mechanism (S6). This selectivity enables SSMs to dynamically aggregate global context in a manner analogous to attention, a connection that Mamba-2 [8] subsequently formalised through the State Space Duality (SSD) framework. While these advances firmly establish SSMs as powerful sequence modellers, their underlying mathematical formulations remain inherently one-dimensional.

Consequently, adapting Mamba for visual tasks has primarily involved flattening 2D images into 1D sequences. Vision Mamba [52], for instance, applies bidirectional 1D scanning within an isotropic architecture. Conversely, VMamba [26] introduces a cross-scan module that processes four directional scans within a hierarchical design. Other variations of this theme include EfficientVMamba [32] with atrous scanning, PlainMamba [43] exploring non-hierarchical structures, and LocalMamba [22] restricting scans to local windows.

Despite their structural diversity, all of these flattening approaches suffer from a fundamental limitation: they destroy the native 2D spatial relationships between neighbouring patches. Because the recurrent memory of an SSM provides exponentially decaying recall over sequence distance, patches that are spatially adjacent but sequentially distant receive disproportionately weak coupling. While employing multiple scan directions can partially compensate for this loss of locality, it merely masks the underlying problem while adding significant computational redundancy.

A smaller body of work has attempted to extend SSMs directly into two spatial dimensions. Early efforts like S4ND [31] generalised S4 to multiple dimensions but retained linear time-invariant parameters, thereby sacrificing the crucial input-dependent selectivity of Mamba. More recently, V2M [38,39] and 2DMamba [48] proposed 2D selective scan formulations, yet in practice, both decompose the operation into sequential horizontal and vertical 1D passes. VSSD [33] takes an alternative approach by removing the causal mask from the SSD framework. This collapses the recurrence into a global weighted sum over all tokens, effectively abandoning sequential scanning in favour of a mechanism closer to linear attention.

Ultimately, none of these methods derive a truly native, selective 2D SSM from first principles; they either reduce to compositions of 1D scans or dispense with recurrent scanning entirely.

3 Method

3.1 Preliminaries

State-Space Models. SSMs describe a 1D mapping from the continuous signal $x(t) : \mathbb{R} \rightarrow \mathbb{R}$ to $y(t) : \mathbb{R} \rightarrow \mathbb{R}$ through an N-D hidden state $h(t) : \mathbb{R} \rightarrow \mathbb{R}^N$. Such a model is parametrised by two projection matrices to and from the latent space ($\mathbf{B} \in \mathbb{R}^{N \times 1}$, $\mathbf{C} \in \mathbb{R}^{1 \times N}$) and an evolution matrix $\mathbf{A} \in \mathbb{R}^{N \times N}$. The full system is then formulated as linear ordinary differential equations (ODEs)

$$\begin{aligned} h'(t) &= \mathbf{A}h(t) + \mathbf{B}x(t), \\ y(t) &= \mathbf{C}h(t) + \mathbf{D}x(t), \end{aligned} \tag{1}$$

where $h'(t)$ is the derivative of the hidden state at time t , and \mathbf{D} is a skip parameter that allows the input to directly influence the output. Although the underlying dynamics are continuous, observations exist only at discrete intervals. We discretise using the Zero Order Hold (ZOH) rule [14]:

$$\bar{\mathbf{A}} = \exp(\Delta\mathbf{A}) \quad \bar{\mathbf{B}} = (\Delta\mathbf{A})^{-1}(\exp(\Delta\mathbf{A}) - \mathbf{I}) \cdot \Delta\mathbf{B}, \tag{2}$$

where Δ is a learnable step size controlling the influence of each input token on the hidden state. This yields a discrete-time recurrence,

$$\begin{aligned} h_t &= \bar{\mathbf{A}}h_{t-1} + \bar{\mathbf{B}}x_t, \\ y_t &= \mathbf{C}h_t + \mathbf{D}x_t, \end{aligned} \tag{3}$$

which scales linearly in complexity with sequence length.

Early SSMs suffered from poor initialization of \mathbf{A} , causing gradients to scale exponentially with sequence length [14]. Modern SSMs address this via the HiPPO theory of continuous-time memorization [13], allowing the state to integrate recent inputs with much higher fidelity than those further in the past.

S6/Mamba employs an input-dependent parametrisation to address the context-based reasoning challenges encountered by its predecessors. To do so, the model learns time-varying functions $\mathbf{B}_t = S_{\mathbf{B}}(x_t)$, $\mathbf{C}_t = S_{\mathbf{C}}(x_t)$, $\Delta_t = \tau_{\Delta}(\Delta + S_{\Delta}(x_t))$ that transform the input elements into said parameters.

3.2 Methodology

Our reformulation of Mamba for 2D inputs partly follows S4ND, initialising two independent sets of axis-specific parameters (*i.e.* $\mathbf{A}_t, \mathbf{B}_t, \Delta_t$ and $\mathbf{A}_z, \mathbf{B}_z, \Delta_z$), with output parameters \mathbf{C} and \mathbf{D} shared across both axes. However, we contrast with S4ND in two key respects. First, S4ND constructs its 2D output by

taking the outer product of two independent 1D SSM transfer functions, which constrains the 2D hidden state to a rank-1 product of separate row and column states. Our formulation instead uses additive joint recurrence, where $h(t, z)$ is simultaneously influenced by both $h(t - 1, z)$ and $h(t, z - 1)$, enabling richer cross-axis interactions that cannot be expressed as a product of independent 1D states. Furthermore, S4ND is restricted to linear-time-invariant parameters, whereas our formulation inherits the input-dependent selectivity of Mamba, allowing the model to dynamically modulate information flow based on content.

Formally, we extend Equation (1) to a 2D domain by introducing two independent partial derivatives (h'_t and h'_z):

$$h'_t(t, z) = \mathbf{A}_t h(t, z) + \mathbf{B}_t x(t, z), \quad (4)$$

$$h'_z(t, z) = \mathbf{A}_z h(t, z) + \mathbf{B}_z x(t, z). \quad (5)$$

We form the discrete recurrence by applying ZOH discretisation along each spatial axis. Since each partial derivative (Equations (4) and (5)) governs dynamics along a single axis, the standard 1D ZOH derivation [14] applies directly to each, giving

$$h(t + \Delta_t, z) = \overline{\mathbf{A}}_t h(t, z) + \overline{\mathbf{B}}_t x(t, z), \quad (6)$$

$$h(t, z + \Delta_z) = \overline{\mathbf{A}}_z h(t, z) + \overline{\mathbf{B}}_z x(t, z), \quad (7)$$

where $\overline{\mathbf{A}}_t = \exp(\Delta_t \mathbf{A}_t)$ and $\overline{\mathbf{B}}_t = \Delta_t \mathbf{B}_t$ (and similarly for z), following the simplified ZOH convention of [12].

This formulation yields two independent recurrences for the same hidden state (from above via Equation (6) and from the left via Equation (7)), whose relative contributions are modulated by the input-dependent selective parameters $\overline{\mathbf{A}}_{t,z}$ and $\overline{\mathbf{B}}_{t,z}$ without the need for a separate learned combination coefficient. We combine the two contributions with a fixed $\frac{1}{2}$ factor for recurrence stability. This results in our 2D SSM equations:

$$h(t, z) = \frac{1}{2} \left(\begin{bmatrix} \overline{\mathbf{A}}_t \\ \overline{\mathbf{A}}_z \end{bmatrix}^\top \begin{bmatrix} h(t - \Delta_t, z) \\ h(t, z - \Delta_z) \end{bmatrix} + \begin{bmatrix} x(t, z) \\ x(t, z) \end{bmatrix}^\top \begin{bmatrix} \overline{\mathbf{B}}_t \\ \overline{\mathbf{B}}_z \end{bmatrix} \right), \quad (8)$$

$$y(t, z) = \mathbf{C}h(t, z) + \mathbf{D}x(t, z). \quad (9)$$

The influence of each 2D input element on each 2D output element is thus determined solely by the Manhattan distance between those points, rather than the distance along any arbitrary 1D flattening of the data.

To address the causal bias of SSMs, we alternate scan direction (top-left-to-bottom-right vs. bottom-right-to-top-left) between subsequent blocks [52], capturing bidirectional spatial context without duplicating computation by using multiple scan directions within a block (ablated in Section 5.3).

3.3 CUDA 2D Wavefront Scan

The associative scan of 1D Mamba cannot be directly extended to parallelise this 2D recurrence, because cumulative multiplication of $\bar{\mathbf{A}}_t$ and $\bar{\mathbf{A}}_z$ creates an intractable number of cross-diagonal paths. We therefore implement wavefront parallelism (Figure 1(a)), computing all elements along a diagonal in parallel via a custom CUDA kernel (Section 3.3), while subsequent diagonals are processed sequentially. We show empirically that this wavefront scan enables compelling throughput and accuracy gains (Section 4.2, Section 5.1).

More formally, within our scan each hidden state $h(t, z)$ depends only on its top $h(t-1, z)$ and left $h(t, z-1)$ neighbours (see Figure 1(a)). As such, all states along a diagonal (where $t+z=d$) are independent of each other and can be computed in parallel.

We dispatch diagonal kernels sequentially from $d=0$ to $H+W-2$, where H and W denote the spatial dimensions of the input. Each kernel computes Equation (8) for all elements within the current diagonal and writes the result to the output tensor h . This dispatch order ensures that the necessary dependencies from the previous wavefront are already committed to global memory before the next kernel begins execution.

Following [12], scan operators are memory-bound due to the low arithmetic intensity of the element-wise recurrence. To mitigate this, our CUDA kernels fuse the discretisation step: rather than materialising $\bar{\mathbf{A}}_{t,z}$ and $\bar{\mathbf{B}}_{t,z}$ in global memory, we compute $\exp(\Delta \cdot A)$ and $\Delta \cdot B \cdot x$ on-the-fly in registers from the projected continuous-time parameters. We additionally avoid storing the hidden states $\mathbf{h} \in \mathbb{R}^{B \times H \times W \times E \times N}$ during training, instead recomputing them during backpropagation; we quantify the impact of both strategies in Section C.

3.4 Mamba2D Model

Block Structure. We employ a MetaFormer-style [44] block structure, transforming an input batch $x \in \mathbb{R}^{B \times H \times W \times C}$ to activations $y \in \mathbb{R}^{B \times H \times W \times C}$ as follows:

$$\begin{aligned} \hat{x} &= \text{Mixer}(\text{Norm}(x)) + x, \\ y &= \text{MLP}(\text{Norm}(\hat{x})) + \hat{x}, \end{aligned} \tag{10}$$

where Norm and Mixer denote our choices of normalisation layer (*i.e.* Layer-Norm) and token-mixer (discussed below) respectively, while MLP denotes a 2-layer MLP with a GELU non-linearity.

Mamba2D Mixer. We adapt the Mamba token-mixer [12] for visual tasks by removing the symmetric gating branch, which is rendered redundant by M2D-SSM’s own selectivity. In its place, we introduce a local processing path using a depthwise separable convolution. Similarly to the 1D convolution used in [17], this provides local spatial priors that complement long-range SSM modelling and improve model convergence.

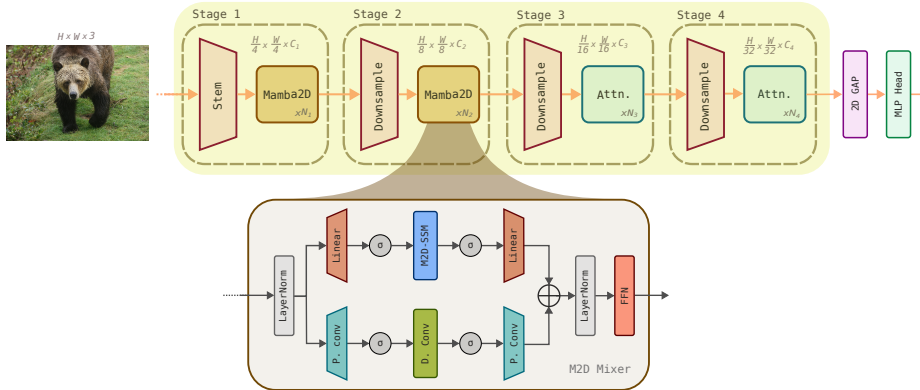


Fig. 2. Mamba2D model architecture. A convolutional stem performs patch embedding, followed by four stages of feature extraction. Each stage consists of $N_{1..4}$ blocks, comprising a token mixer and an FFN. The Mamba2D token mixer uses two parallel branches: our native 2D SSM path and a local processing path, whose outputs are combined before the FFN.

Table 1. Architecture configurations of Mamba2D model variants. *Note: DP Rate refers to Drop Path rate (stochastic depth).*

Model	Blocks	Channels	DP Rate	Dropout	#Param.	FLOPs
M2D-N	[3, 3, 9, 3]	[32, 64, 160, 256]	0.000	0.00	7.2M	1.35G
M2D-T	[3, 3, 9, 3]	[64, 128, 320, 512]	0.175	0.15	26.5M	4.66G
M2D-S	[3, 12, 14, 3]	[96, 192, 384, 576]	0.400	0.40	50.3M	13.74G

Overall Architecture. We implement the Mamba2D mixer described above as a choice of token mixer within a hierarchical structure inspired by the baselines laid out in MetaFormer (see Figure 2). As such, our overall model consists of four stages comprising a strided convolution-based stem/downsample followed by $N_{1..4}$ mixer blocks within each stage and a post-stage LayerNorm.

For the task of classification, we employ Global Average Pooling (GAP) before feeding the features to an MLP classification head. The attention layers adopt QK-normalisation (QK-Norm) [19] and Rotary Position Embedding (RoPE) [35] for training stability. We ablate the hybrid stage configuration in Section 5.1.

4 Experiments

We train the model variants in Table 1 on ImageNet-1K [9] for 300 epochs following standard practices [36,29,26]. Full training details are provided in Section A. We additionally evaluate on MS-COCO [25] object detection and ADE20K [51] segmentation.

Table 2. Top-1 accuracy on ImageNet-1K. **Left:** attention-based and 1D-SSM methods. **Right:** convolutional networks and 2D-SSM methods, including our M2D (bold). Results sorted by parameter count within each group. Within each model size group we highlight the **1st** / **2nd** / **3rd** best; highlight width reflects model scale.

Model	#Param.	Top-1 (%)	Model	#Param.	Top-1 (%)
<i>Attention</i>			<i>Convolutional</i>		
DeiT-S [37]	22 M	79.8	ConvNeXt-T [30]	26 M	82.1
Swin-T [28]	29 M	81.3	ConvNeXt-S [30]	50 M	83.1
SwinV2-T [27]	29 M	81.8	ConvNeXt-B [30]	89 M	83.8
Swin-S [28]	50 M	83.2	<i>2D SSM</i>		
SwinV2-S [27]	50 M	83.8	V2M-T [38]	7 M	76.2
DeiT-B [37]	86 M	81.8	VSSD-M [33]	14 M	82.5
Swin-B [28]	88 M	83.5	VSSD-T [33]	24 M	83.7
SwinV2-B [27]	88 M	84.6	V2M-S [38]	26 M	80.5
<i>1D SSM</i>			S4ND-ConvNeXt-B [31]	30 M	82.2
ViM-Ti [52]	7 M	76.1	2DVMamba-T [49]	30 M	82.8
ViM-S [52]	26 M	80.3	V2M-S* [38]	30 M	82.9
LocalVMamba-T [22]	26 M	82.7	VSSD-S [33]	40 M	84.1
VMamba-T [26]	30 M	82.6	2DVMamba-S [49]	50 M	83.8
MambaVision-T [17]	32 M	82.3	V2M-B* [38]	50 M	83.8
EfficientVMamba-B [32]	33 M	81.8	VSSD-B [33]	89 M	84.7
MambaVision-S [17]	50 M	83.3	M2D-N		
VMamba-S [26]	50 M	83.6		7 M	79.6
VMamba-B [26]	89 M	83.9	M2D-T	27 M	84.0
MambaVision-B [17]	98 M	84.2	M2D-S	50 M	85.3

4.1 Image Classification on ImageNet-1K

Table 2 presents ImageNet-1K classification results. M2D achieves state-of-the-art performance across all model scales: our M2D-T (27M) reaches 84.0%, surpassing the previous best 2D-SSM VSSD-T (83.7%) and all 1D-SSM and attention-based models of comparable size, including several larger models such as VMamba-T (30M, 82.6%) and EfficientVMamba-B (33M, 81.8%). Our M2D-S (50M) also achieves 85.3%, outperforming VMamba-S (83.6%) and V2M-B (83.8%) by substantial margins.

4.2 Computational Efficiency and Scalability

As shown in Figure 3, M2D scales sub-linearly in latency ($O(N^{0.56})$) due to the wavefront’s diagonal-depth growth of $O(\sqrt{N})$. At an input size of 1024^2 it is $\sim 50\times$ faster than Flash Attention [7], $\sim 2.5\times$ faster than VMamba SS2D, and $\sim 4\times$ faster than V2M, while all SSM-based operators maintain linear memory scaling.

For brevity, the full operator comparison and per-strategy recomputation breakdowns are provided in Sections B and C respectively. However, in summary we note that the fusion and recomputation strategies of Section 3.3 capitalise on the memory-bound nature of the scan, and partial recomputation reduces peak VRAM by $\sim 81\%$ while simultaneously reducing forward+backward wall time by $\sim 37\%$ and forward-only time by $\sim 54\%$. Full recomputation reaches $\sim 10\%$ of

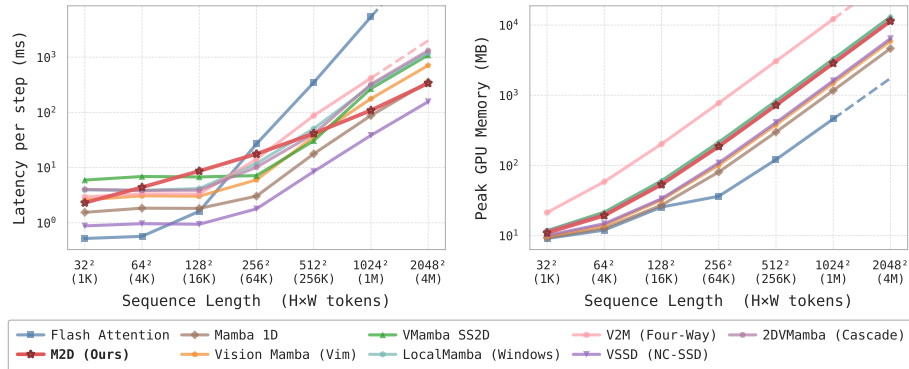


Fig. 3. Kernel-level scaling of nine token-mixing operators across spatial resolutions (32^2 – 2048^2). *Left:* forward-pass latency (ms, log scale). *Right:* peak GPU memory (MB, log scale). Dashed lines denote log-log extrapolations: Flash Attention [7] is capped at 1024^2 due to intractable runtime; V2M runs out of memory at 2048^2 .

the naive VRAM footprint at a marginal $\sim 2\%$ latency overhead, making high-resolution inference and training tractable.

4.3 Object Detection and Instance Segmentation

For object detection and instance segmentation, we fine-tune Mask R-CNN [11] on MS-COCO [25] using MMDetection [3] under $1\times$ and $3\times$ schedules. Full training details are in Section A.

As shown in Tables 3 and 4, M2D-T and M2D-S set a new state-of-the-art among 2D-SSM backbones at both training schedules, with competitive results at the nano scale. Under the $1\times$ schedule, M2D-T (44M) reaches 48.5/43.8 box/mask AP, leading V2M-S* (47.6), VMamba-T (47.3), and VSSD-T (46.9) by 0.9–1.6 box AP while using fewer parameters (44M vs. 44–50M). M2D-S reaches 50.4/45.1, outperforming V2M-B* (48.9), VMamba-S (48.7), and VSSD-S (48.4) by 1.5–2.0 box AP, while M2D-N delivers competitive results at substantially lower FLOPs (175G vs. 197–220G). Under the $3\times$ schedule, M2D-T advances to 50.5/44.7, extending its lead by 1.5–1.7 box AP over prior SSM-based backbones, with gains consistent across box and mask metrics. M2D-S further reaches 52.2/46.2, surpassing V2M-B* (50.0) and VMamba-S (49.9) by 2.2 and 2.3 box AP respectively, establishing state-of-the-art performance among all SSM-based backbones at the small scale.

4.4 Semantic Segmentation

For semantic segmentation on ADE20K [51], we employ UperNet [42] with MM-Segmentation [4], evaluating under both single-scale (SS) and multi-scale (MS) settings. Full training details are in Section A.

Table 3. Object detection and instance segmentation results on MS-COCO with Mask R-CNN using $1\times$ schedule. FLOPs are estimated at input resolution 1280×800 . Within each model size group we highlight the **1st** / **2nd** / **3rd** best; highlight width reflects model scale.

Backbone	AP ^b	AP ^b ₅₀	AP ^b ₇₅	AP ^m	AP ^m ₅₀	AP ^m ₇₅	#param.	FLOPs
PVT-T [40]	36.7	59.2	39.3	35.1	56.7	37.3	33 M	208 G
EffVMamba-S [32]	39.3	61.8	42.8	36.7	58.9	39.2	31 M	197 G
M2D-N	42.8	65.3	46.7	39.6	62.5	42.5	26 M	175 G
MSVMamba-M [34]	43.8	65.8	47.7	39.9	62.9	42.9	32 M	201 G
VSSD-M [33]	45.4	67.5	49.8	41.3	64.5	44.6	33 M	220 G
ResNet-50 [18]	38.2	58.8	41.4	34.7	55.7	37.2	44 M	260 G
Swin-T [28]	42.7	65.2	46.8	39.3	62.2	42.2	48 M	267 G
ConvNeXt-T [30]	44.2	66.6	48.3	40.1	63.3	42.8	48 M	262 G
VSSD-T [33]	46.9	69.4	51.4	42.6	66.4	45.9	44 M	265 G
VMamba-T [26]	47.3	69.3	52.0	42.7	66.4	45.9	50 M	271 G
V2M-S* [38]	47.6	69.4	52.2	42.9	66.5	46.3	50 M	-
M2D-T	48.5	71.0	53.1	43.8	67.8	47.1	44 M	288 G
ResNet-101 [18]	40.4	61.1	44.2	36.4	58.1	38.8	63 M	336 G
Swin-S [28]	44.8	66.6	48.9	40.9	63.2	44.2	69 M	354 G
ConvNeXt-S [30]	45.4	67.9	50.0	41.8	65.0	45.1	70 M	348 G
VSSD-S [33]	48.4	70.1	53.1	43.5	67.2	47.1	59 M	325 G
VMamba-S [26]	48.7	70.0	53.4	43.7	67.3	47.0	70 M	349 G
V2M-B* [38]	48.9	70.2	53.6	43.8	67.5	47.1	70 M	-
M2D-S	50.4	72.3	55.3	45.1	69.4	48.6	67 M	549 G

Table 4. Object detection and instance segmentation results on MS-COCO with Mask R-CNN using $3\times$ multi-scale schedule. FLOPs are estimated at input resolution 1280×800 . Within each model size group we highlight the **1st** / **2nd** / **3rd** best; highlight width reflects model scale.

Backbone	AP ^b	AP ^b ₅₀	AP ^b ₇₅	AP ^m	AP ^m ₅₀	AP ^m ₇₅	#param.	FLOPs
PVT-T [40]	39.8	62.2	43.0	37.4	59.3	39.9	33 M	208 G
LightViT-T [21]	41.5	64.4	45.1	38.4	61.2	40.8	28 M	187 G
EffVMamba-S [32]	41.6	63.9	45.6	38.2	60.8	40.7	31 M	197 G
MSVMamba-M [34]	46.3	68.1	50.8	41.8	65.1	44.9	32 M	201 G
M2D-N	47.2	69.2	51.7	42.4	65.9	45.6	26 M	175 G
VSSD-M [33]	47.7	69.7	52.1	42.8	66.5	46.0	33 M	220 G
ResNet-50 [18]	41.0	61.7	44.9	37.1	58.4	40.1	44 M	260 G
Swin-T [28]	46.0	68.1	50.3	41.6	65.1	44.9	48 M	267 G
ConvNeXt-T [30]	46.2	67.9	50.8	41.7	65.0	44.9	48 M	262 G
VSSD-T [33]	48.8	70.4	53.6	43.6	67.6	46.9	44 M	265 G
VMamba-T [26]	48.8	70.4	53.5	43.7	67.4	47.0	50 M	271 G
V2M-S* [38]	49.0	70.6	53.5	43.8	67.5	47.2	50 M	-
M2D-T	50.5	72.1	55.4	44.7	68.9	48.3	44 M	288 G
ResNet-101 [18]	42.8	63.2	47.1	38.5	60.1	41.4	63 M	336 G
Swin-S [28]	48.2	69.8	52.8	43.2	67.0	46.1	69 M	354 G
ConvNeXt-S [30]	47.9	69.0	52.7	42.9	66.9	46.2	70 M	348 G
VMamba-S [26]	49.9	70.9	54.7	44.2	68.2	47.7	70 M	349 G
V2M-B* [38]	50.0	70.9	54.8	44.3	68.4	47.8	70 M	-
M2D-S	52.2	73.1	57.4	46.2	70.6	50.4	67 M	549 G

Table 5. Semantic segmentation results on ADE20K with UperNet. FLOPs are estimated at crop size 512×2048 . Within each model size group we highlight the **1st** / **2nd** / **3rd** best; highlight width reflects model scale.

Backbone	#Param.	FLOPs	mIoU (SS)	mIoU (MS)
Vim-Ti [52]	13 M	–	41.0	–
V2M-T [38]	13 M	–	41.4	42.0
EfficientVMamba-S [32]	29 M	505 G	41.5	42.1
M2D-N	34 M	355 G	43.1	43.1
LocalVim-T [22]	36 M	260 G	43.4	44.4
ResNet-50 [18]	66 M	953 G	42.1	42.8
Swin-T [28]	60 M	945 G	44.4	45.8
Vim-S [52]	46 M	–	44.9	–
V2M-S [38]	46 M	482 G	45.1	46.1
MSVMamba-M [34]	42 M	875 G	45.1	45.4
VSSD-M [33]	42 M	893 G	45.6	46.0
EffVMamba-B [32]	65 M	930 G	46.5	47.3
MSVMamba-T [34]	65 M	942 G	47.6	48.5
VSSD-T [33]	53 M	941 G	47.9	48.7
VMamba-T [26]	62 M	948 G	47.9	48.8
V2M-S* [38]	62 M	482 G	48.2	49.0
M2D-T	53 M	485 G	48.9	49.3
ResNet-101 [18]	85 M	1030 G	44.9	45.9
Swin-S [28]	81 M	1039 G	47.6	49.5
NAT-S [16]	82 M	1010 G	48.0	49.5
2DMamba [49]	92 M	950 G	48.6	49.3
ConvNeXt-S [30]	82 M	1028 G	48.7	49.6
VMamba-S [26]	82 M	1028 G	50.6	51.2
V2M-B* [38]	82 M	655 G	50.8	51.3
M2D-S	77 M	768 G	51.7	51.8

As shown in Table 5, M2D-T and M2D-S set a new state-of-the-art among SSM-based approaches at substantially lower FLOPs. M2D-T reaches 48.9 SS mIoU, leading VMamba-T (47.9) and VSSD-T (47.9) at roughly half their FLOPs (485G vs. 941–948G), and V2M-S* (48.2) at comparable cost. M2D-S advances to 51.7, surpassing V2M-B* (50.8), VMamba-S (50.6), and 2DMamba (48.6) by margins of 0.9, 1.1, and 3.1 points respectively. M2D-N delivers competitive results at lower FLOPs (355G vs. 482–505G). Both M2D-T (49.3) and M2D-S (51.8) maintain their leads under multi-scale evaluation.

5 Ablations

To explore our design choices, we ablate M2D-N following the training setup of Section 4. Following standard practice, high-level architectural decisions (stage-wise mixer selection) are evaluated on ImageNet-1K classification accuracy and

Table 6. Ablation of stage-wise token mixer selection on ImageNet-1K (M2D-N architecture). Top-1 accuracy (300-epoch) and inference throughput.

Config	Acc. (%)	Throughput (images/sec)						
		224 ²	512 ²	1024 ²	1536 ²	2048 ²	2560 ²	3072 ²
4M 0A	78.6	120.7	92.2	49.7	30.8	<i>20.3</i>	<i>14.3</i>	<i>10.6</i>
3M 1A	78.9	113.8	86.2	51.0	<i>31.7</i>	<i>20.7</i>	14.6	10.8
2M 2A	79.6	113.2	<i>95.5</i>	<i>62.9</i>	36.3	22.5	<i>14.4</i>	<i>9.3</i>
1M 3A	79.7	<i>114.2</i>	102.8	70.8	<i>35.6</i>	18.6	10.3	5.8
0M 4A	<i>79.4</i>	<i>120.4</i>	123.0	<i>56.9</i>	17.7	6.0	2.6	1.3

throughput. Design choices with broader impact (*e.g.* component contributions and scan patterns) are additionally validated on downstream dense prediction benchmarks. All throughput measurements use bfloat16 inference on an NVIDIA RTX 5090.

5.1 Stage-wise Token Mixer Selection

Table 6 and Figure 4 report ImageNet-1K accuracy and throughput for M2D-N with varying proportions of Mamba2D (M) and attention (A) stages across the four network stages; configurations are denoted $xMyA$.

Accuracy saturates beyond 2M2A (79.6%), with 1M3A adding only 0.1% at significant throughput cost. The crossover at input size 1536² (Figure 4, right) shows 2M2A surpassing all higher-attention configurations. At 2048² inputs, it is 21% faster than 1M3A and 3.8× faster than 0M4A. This validates our design: by restricting attention to later stages where spatial dimensions are small, we extract its modelling benefits without incurring quadratic costs. This motivates the 2M2A configuration used throughout our experiments.

5.2 Mamba2D Mixer Components

Table 7 evaluates the contribution of each parallel path in the Mamba2D mixer: the native 2D SSM path and the local depthwise separable convolution path.

As expected from prior work [45], both paths contribute minimally to classification accuracy (79.4–79.6% regardless of configuration). However, on dense prediction tasks the paths are complementary. The local path captures texture and boundary information (the primary signal for per-pixel segmentation), explaining the larger 1.3 mIoU drop when it is removed. Detection requires integrating spatial context across larger regions to localise instances, where the long-range M2D scan is better suited, causing a 1.7 AP^b drop when removed, compared to only 0.9 AP^b when the local path is removed. Removing the M2D path entirely marginally outperforms retaining the projections without the scan (41.3 vs. 41.1 AP^b), confirming that the SSM projections are only useful in conjunction with the scan. The full model achieves the best performance across all tasks.

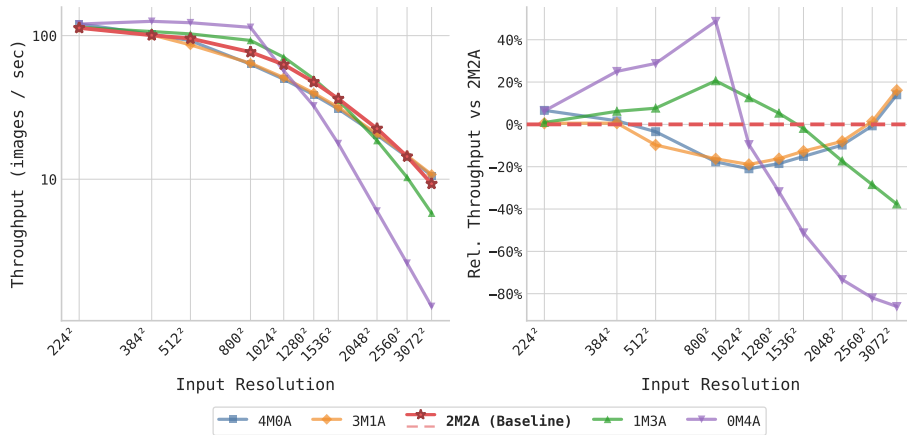


Fig. 4. Throughput vs input resolution for different stage-wise mixer configurations. **Left:** Absolute throughput on log-log scale. **Right:** Relative performance vs 2M2A baseline. The crossover at 1536^2 resolution (147K tokens) shows M2D’s superior scaling at high resolution, while pure attention (0M4A) exhibits quadratic degradation.

Table 7. Ablation of Mamba2D mixer components. We report ImageNet-1K Top-1 accuracy, MS-COCO object detection metrics ($1\times$ schedule), and ADE20K semantic segmentation mIoU (single-scale).

Configuration	Top-1 (%)	AP ^b	AP ^m	mIoU
Baseline (full)	79.6	42.8	39.6	43.1
w/o local path	79.4	41.9	39.0	41.8
w/o M2D scan	79.6	41.1	38.4	<u>42.8</u>
w/o M2D path (conv only)	79.4	41.3	38.4	42.6

5.3 Scan Direction Strategies

We evaluate scanning strategies that vary the number of directions and whether directions are alternate between blocks (no extra overhead) or duplicated within each block (proportionally more compute). The baseline (top-left to bottom-right, TL→BR) follows the natural wavefront order of the 2D recurrence. Table 8 reports accuracy and relative throughput.

Single-direction scanning (TL→BR) incurs a meaningful detection drop (41.8 vs. 42.8 AP^b) due to directional bias. 2-dir alternating recovers this at no throughput cost. Increasing this to 4-dir alternating provides no further benefit, as two complementary directions already capture the bidirectional spatial context required by dense prediction tasks. Per-block strategies reach marginally higher peak scores (43.0 AP^b, 43.9 mIoU), though the throughput penalties (0.65× and 0.38×) are not justified by the modest gains. We therefore adopt 2-dir alternating as our default scan strategy.

Table 8. Ablation of scan direction strategies. Alternating strategies alternate scan direction between blocks with no additional scan overhead, while per-block strategies run multiple scans within each block. Relative throughput is normalised to the 2-dir alternating baseline. We report ImageNet-1K Top-1 accuracy, MS-COCO AP (1× schedule), and ADE20K mIoU (single-scale).

Scan Strategy	Throughput	Top-1 (%)	AP ^b	AP ^m	mIoU
TL→BR only	1.01×	79.8	41.8	38.9	42.9
2-dir alternating (baseline)	1.00×	79.6	42.8	39.6	43.1
2-dir per block	0.65×	79.7	43.0	39.8	42.7
4-dir alternating	1.00×	79.7	42.7	39.5	42.9
4-dir per block	0.38×	80.0	42.8	39.6	43.9

6 Conclusion

In this paper, we introduced Mamba2D, a natively multi-dimensional state-space model for vision that derives a true joint 2D SSM from first principles rather than composing or factoring 1D scans. To make this tractable, we implement and release a custom CUDA wavefront-scan kernel that exploits diagonal independence for parallelism, with selective activation recomputation achieving linear memory scaling across high-resolution inputs. The wavefront scan yields sub-linear latency growth in resolution, in contrast to the quadratic scaling of attention. Our hybrid architecture, combining native 2D SSMs in high-resolution stages with vanilla attention in low-resolution stages, achieved state-of-the-art results among SSM-based models on ImageNet-1K classification, MS-COCO object detection, and ADE20K semantic segmentation at a range of model sizes and operating points.

A current limitation is that the sequential diagonal ordering of the wavefront scan carries a higher constant-factor latency than 1D operators at low spatial resolutions, an overhead that is amortised at the high resolutions where M2D is most naturally deployed. Future work may explore hardware-aware diagonal scheduling to further reduce the constant-factor latency overhead at low spatial resolutions. More broadly, the wavefront formulation extends naturally beyond 2D, offering a principled path towards natively volumetric state-space models for tasks such as video understanding and medical imaging, as well as event-based visual sensing where SSMs have already shown promise [20].

References

1. Bochkovskii, A., Delaunoy, A., Germain, H., Santos, M., Zhou, Y., Richter, S.R., Koltun, V.: Depth pro: Sharp monocular metric depth in less than a second. In: International Conference on Learning Representations (2025)
2. Carion, N., Massa, F., Synnaeve, G., Usunier, N., Kirillov, A., Zagoruyko, S.: End-to-end object detection with transformers. In: European Conference on Computer Vision. pp. 213–229. Springer (2020)
3. Chen, K., Wang, J., Pang, J., Cao, Y., Xiong, Y., Li, X., Sun, S., Feng, W., Liu, Z., Xu, J., Zhang, Z., Cheng, D., Zhu, C., Cheng, T., Zhao, Q., Li, B., Lu, X., Zhu, R., Wu, Y., Dai, J., Wang, J., Shi, J., Ouyang, W., Loy, C.C., Lin, D.: MMDetection: Open mmlab detection toolbox and benchmark. arXiv preprint arXiv:1906.07155 (2019)
4. Contributors, M.: MMsegmentation: Openmmlab semantic segmentation toolbox and benchmark. <https://github.com/open-mmlab/msegmentation> (2020)
5. Cubuk, E.D., Zoph, B., Shlens, J., Le, Q.: Randaugment: Practical automated data augmentation with a reduced search space. In: Larochelle, H., Ranzato, M., Hadsell, R., Balcan, M., Lin, H. (eds.) Advances in Neural Information Processing Systems. vol. 33, pp. 18613–18624. Curran Associates, Inc. (2020), https://proceedings.neurips.cc/paper_files/paper/2020/file/d85b63ef0ccb114d0a3bb7b7d808028f-Paper.pdf
6. Dai, Z., Liu, H., Le, Q.V., Tan, M.: CoAtNet: Marrying convolution and attention for all data sizes. In: Advances in Neural Information Processing Systems. vol. 34, pp. 3339–3349. Curran Associates, Inc. (2021)
7. Dao, T., Fu, D., Ermon, S., Rudra, A., Ré, C.h.: Flashattention: Fast and memory-efficient exact attention with io-awareness. In: Koyejo, S., Mohamed, S., Agarwal, A., Belgrave, D., and A. Oh, K.C. (eds.) Advances in Neural Information Processing Systems. vol. 35, pp. 16344–16359. Curran Associates, Inc. (2022), https://proceedings.neurips.cc/paper_files/paper/2022/file/67d57c32e20fd0a7a302cb81d36e40d5-Paper-Conference.pdf
8. Dao, T., Gu, A.: Transformers are SSMs: Generalized models and efficient algorithms through structured state space duality. In: Proceedings of the 41st International Conference on Machine Learning. Proceedings of Machine Learning Research, vol. 235, pp. 10041–10071. PMLR (2024)
9. Deng, J., Dong, W., Socher, R., Li, L.J., Li, K., Fei-Fei, L.: Imagenet: A large-scale hierarchical image database. In: 2009 IEEE Conference on Computer Vision and Pattern Recognition. pp. 248–255 (2009). <https://doi.org/10.1109/CVPR.2009.5206848>
10. Dosovitskiy, A., Beyer, L., Kolesnikov, A., Weissenborn, D., Zhai, X., Unterthiner, T., Dehghani, M., Minderer, M., Heigold, G., Gelly, S., Uszkoreit, J., Houshy, N.: An image is worth 16x16 words: Transformers for image recognition at scale. In: International Conference on Learning Representations (2021)
11. Girshick, R., Radosavovic, I., Gkioxari, G., Dollár, P., He, K.: Detectron. <https://github.com/facebookresearch/detectron> (2018)
12. Gu, A., Dao, T.: Mamba: Linear-Time Sequence Modeling with Selective State Spaces (Dec 2023)
13. Gu, A., Dao, T., Ermon, S., Rudra, A., Re, C.: HiPPO: Recurrent memory with optimal polynomial projections. In: Advances in Neural Information Processing Systems. vol. 33, pp. 1474–1487. Curran Associates, Inc. (2020)

14. Gu, A., Goel, K., Ré, C.: Efficiently modeling long sequences with structured state spaces. In: International Conference on Learning Representations (2022)
15. Guo, J., Han, K., Wu, H., Tang, Y., Chen, X., Wang, Y., Xu, C.: CMT: Convolutional neural networks meet vision transformers. In: Proceedings of the IEEE/CVF Conference on Computer Vision and Pattern Recognition (CVPR). pp. 12175–12185 (2022)
16. Hassani, A., Walton, S., Li, J., Li, S., Shi, H.: Neighborhood attention transformer. In: 2023 IEEE/CVF Conference on Computer Vision and Pattern Recognition (CVPR). pp. 6185–6194 (2023). <https://doi.org/10.1109/CVPR52729.2023.00599>
17. Hatamizadeh, A., Kautz, J.: MambaVision: A hybrid mamba-transformer vision backbone. In: Proceedings of the IEEE/CVF Conference on Computer Vision and Pattern Recognition (CVPR) (2025)
18. He, K., Zhang, X., Ren, S., Sun, J.: Deep residual learning for image recognition. In: Proceedings of the IEEE Conference on Computer Vision and Pattern Recognition (CVPR). pp. 770–778 (2016)
19. Henry, A., Dachapally, P.R., Pawar, S.S., Chen, Y.: Query-key normalization for transformers. In: Cohn, T., He, Y., Liu, Y. (eds.) Findings of the Association for Computational Linguistics: EMNLP 2020. pp. 4246–4253. Association for Computational Linguistics, Online (Nov 2020). <https://doi.org/10.18653/v1/2020.findings-emnlp.379>, <https://aclanthology.org/2020.findings-emnlp.379/>
20. Hernández Díaz, A., Davidson, R., Eckersley, S., Hadfield, S.: E-mamba: Using state-space-models for direct event processing in space situational awareness (Oct 2024). <https://doi.org/10.5281/zenodo.13885677>, <https://doi.org/10.5281/zenodo.13885677>
21. Huang, T., Huang, L., You, S., Wang, F., Qian, C., Xu, C.: Lightvit: Towards light-weight convolution-free vision transformers. arXiv preprint arXiv:2207.05557 (2022)
22. Huang, T., Pei, X., You, S., Wang, F., Qian, C., Xu, C.: LocalMamba: Visual state space model with windowed selective scan. In: Computer Vision – ECCV 2024 Workshops. Lecture Notes in Computer Science, vol. 15633, pp. 19–36. Springer (2025). https://doi.org/10.1007/978-3-031-91979-4_2
23. Kag, A., Coskun, H., Chen, J., Cao, J., Menapace, W., Siarohin, A., Tulyakov, S., Ren, J.: AsCAN: Asymmetric convolution-attention networks for efficient recognition and generation. In: Advances in Neural Information Processing Systems. vol. 37. Curran Associates, Inc. (2024)
24. Lin, T.Y., Dollar, P., Girshick, R., He, K., Hariharan, B., Belongie, S.: Feature pyramid networks for object detection. In: Proceedings of the IEEE Conference on Computer Vision and Pattern Recognition (CVPR) (July 2017)
25. Lin, T.Y., Maire, M., Belongie, S., Hays, J., Perona, P., Ramanan, D., Dollár, P., Zitnick, C.L.: Microsoft coco: Common objects in context. In: Fleet, D., Pajdla, T., Schiele, B., Tuytelaars, T. (eds.) Computer Vision – ECCV 2014. pp. 740–755. Springer International Publishing, Cham (2014)
26. Liu, Y., Tian, Y., Zhao, Y., Yu, H., Xie, L., Wang, Y., Ye, Q., Jiao, J., Liu, Y.: VMamba: Visual state space model. In: Advances in Neural Information Processing Systems. vol. 37. Curran Associates, Inc. (2024)
27. Liu, Z., Hu, H., Lin, Y., Yao, Z., Xie, Z., Wei, Y., Ning, J., Cao, Y., Zhang, Z., Dong, L., Wei, F., Guo, B.: Swin transformer v2: Scaling up capacity and resolution. In: Proceedings of the IEEE/CVF Conference on Computer Vision and Pattern Recognition (CVPR). pp. 12009–12019 (2022)

28. Liu, Z., Lin, Y., Cao, Y., Hu, H., Wei, Y., Zhang, Z., Lin, S., Guo, B.: Swin transformer: Hierarchical vision transformer using shifted windows. In: Proceedings of the IEEE/CVF International Conference on Computer Vision (ICCV). pp. 10012–10022 (2021)
29. Liu, Z., Lin, Y., Cao, Y., Hu, H., Wei, Y., Zhang, Z., Lin, S., Guo, B.: Swin transformer: Hierarchical vision transformer using shifted windows. In: Proceedings of the IEEE/CVF International Conference on Computer Vision (ICCV). pp. 10012–10022 (2021)
30. Liu, Z., Mao, H., Wu, C.Y., Feichtenhofer, C., Darrell, T., Xie, S.: A ConvNet for the 2020s. In: Proceedings of the IEEE/CVF Conference on Computer Vision and Pattern Recognition (CVPR). pp. 11976–11986 (2022)
31. Nguyen, E., Goel, K., Gu, A., Downs, G.W., Shah, P., Dao, T., Baccus, S.A., Ré, C.: S4ND: Modeling images and videos as multidimensional signals using state spaces. In: Advances in Neural Information Processing Systems. vol. 35, pp. 2846–2861. Curran Associates, Inc. (2022)
32. Pei, X., Huang, T., Xu, C.: EfficientVMamba: Atrous selective scan for light weight visual mamba. In: Proceedings of the AAAI Conference on Artificial Intelligence. pp. 6443–6451 (2025). <https://doi.org/10.1609/aaai.v39i6.32690>
33. Shi, Y., Dong, M., Li, M., Xu, C.: VSSD: Vision mamba with non-causal state space duality. In: Proceedings of the IEEE/CVF International Conference on Computer Vision (ICCV) (2025)
34. Shi, Y., Dong, M., Xu, C.: Multi-scale vmamba: Hierarchy in hierarchy visual state space model. In: Globerson, A., Mackey, L., Belgrave, D., Fan, A., Paquet, U., Tomczak, J., Zhang, C. (eds.) Advances in Neural Information Processing Systems. vol. 37, pp. 25687–25708. Curran Associates, Inc. (2024). <https://doi.org/10.52202/079017-0808>, https://proceedings.neurips.cc/paper_files/paper/2024/file/2d69e771d9f274f7c624198ea74f5b98-Paper-Conference.pdf
35. Su, J., Lu, Y., Pan, S., Murtadha, A., Wen, B., Liu, Y.: RoFormer: Enhanced transformer with rotary position embedding. *Neurocomputing* **568**, 127063 (2024). <https://doi.org/10.1016/j.neucom.2023.127063>
36. Touvron, H., Cord, M., Douze, M., Massa, F., Sablayrolles, A., Jégou, H.: Training data-efficient image transformers & distillation through attention. In: Proceedings of the 38th International Conference on Machine Learning. Proceedings of Machine Learning Research, vol. 139, pp. 10347–10357. PMLR (2021)
37. Touvron, H., Cord, M., Douze, M., Massa, F., Sablayrolles, A., Jégou, H.: Training data-efficient image transformers & distillation through attention. In: Proceedings of the 38th International Conference on Machine Learning. Proceedings of Machine Learning Research, vol. 139, pp. 10347–10357. PMLR (2021)
38. Wang, C., Zheng, W., Huang, Y., Zhou, J., Lu, J.: V2M: Visual 2-Dimensional Mamba for Image Representation Learning (Oct 2024)
39. Wang, C., Zheng, W., Huang, Y., Zhou, J., Lu, J.: V2m: Visual 2-dimensional mamba for image representation learning (2024), <https://arxiv.org/abs/2410.10382>
40. Wang, W., Xie, E., Li, X., Fan, D.P., Song, K., Liang, D., Lu, T., Luo, P., Shao, L.: Pyramid vision transformer: A versatile backbone for dense prediction without convolutions. In: Proceedings of the IEEE/CVF International Conference on Computer Vision (ICCV). pp. 568–578 (2021)
41. Wu, Y., He, K.: Group normalization. In: Ferrari, V., Hebert, M., Sminchisescu, C., Weiss, Y. (eds.) Computer Vision – ECCV 2018. pp. 3–19. Springer International Publishing, Cham (2018)

42. Xiao, T., Liu, Y., Zhou, B., Jiang, Y., Sun, J.: Unified perceptual parsing for scene understanding. In: Ferrari, V., Hebert, M., Sminchisescu, C., Weiss, Y. (eds.) *Computer Vision – ECCV 2018*. pp. 432–448. Springer International Publishing, Cham (2018)
43. Yang, C., Chen, Z., Espinosa, M., Ericsson, L., Wang, Z., Liu, J., Crowley, E.J.: Plainmamba: Improving non-hierarchical mamba in visual recognition. In: 35th British Machine Vision Conference 2024, BMVC 2024, Glasgow, UK, November 25–28, 2024. BMVA (2024)
44. Yu, W., Luo, M., Zhou, P., Si, C., Zhou, Y., Wang, X., Feng, J., Yan, S.: MetaFormer is actually what you need for vision. In: *Proceedings of the IEEE/CVF Conference on Computer Vision and Pattern Recognition (CVPR)*. pp. 10819–10829 (2022)
45. Yu, W., Wang, X.: Mambaout: Do we really need mamba for vision? In: 2025 IEEE/CVF Conference on Computer Vision and Pattern Recognition (CVPR). pp. 4484–4496 (2025). <https://doi.org/10.1109/CVPR52734.2025.00423>
46. Yun, S., Han, D., Chun, S., Oh, S.J., Yoo, Y., Choe, J.: Cutmix: Regularization strategy to train strong classifiers with localizable features. In: 2019 IEEE/CVF International Conference on Computer Vision (ICCV). pp. 6022–6031 (2019). <https://doi.org/10.1109/ICCV.2019.00612>
47. Zhang, H., Cissé, M., Dauphin, Y.N., Lopez-Paz, D.: mixup: Beyond empirical risk minimization. In: 6th International Conference on Learning Representations, ICLR 2018, Vancouver, BC, Canada, April 30 - May 3, 2018, Conference Track Proceedings. OpenReview.net (2018), <https://openreview.net/forum?id=r1Ddp1-Rb>
48. Zhang, J., Nguyen, A.T., Han, X., Trinh, V.Q.H., Qin, H., Samaras, D., Hosseini, M.S.: 2dmamba: Efficient state space model for image representation with applications on giga-pixel whole slide image classification. In: 2025 IEEE/CVF Conference on Computer Vision and Pattern Recognition (CVPR). pp. 3583–3592 (2025). <https://doi.org/10.1109/CVPR52734.2025.00339>
49. Zhang, J., Nguyen, A.T., Han, X., Trinh, V.Q.H., Qin, H., Samaras, D., Hosseini, M.S.: 2DMamba: Efficient state space model for image representation with applications on giga-pixel whole slide image classification. In: *Proceedings of the IEEE/CVF Conference on Computer Vision and Pattern Recognition (CVPR)* (2025)
50. Zhong, Z., Zheng, L., Kang, G., Li, S., Yang, Y.: Random erasing data augmentation. In: *Proceedings of the AAAI Conference on Artificial Intelligence (AAAI)* (2020)
51. Zhou, B., Zhao, H., Puig, X., Fidler, S., Barriuso, A., Torralla, A.: Scene parsing through ade20k dataset. In: 2017 IEEE Conference on Computer Vision and Pattern Recognition (CVPR). pp. 5122–5130 (2017). <https://doi.org/10.1109/CVPR.2017.544>
52. Zhu, L., Liao, B., Zhang, Q., Wang, X., Liu, W., Wang, X.: Vision mamba: Efficient visual representation learning with bidirectional state space model. In: *Proceedings of the 41st International Conference on Machine Learning. Proceedings of Machine Learning Research*, vol. 235, pp. 62429–62442. PMLR (2024)

Appendices

A Training and Implementation Details

Table 9 summarises the training hyperparameters and implementation details for all three benchmarks. All unspecified hyperparameters follow the default settings of the respective framework.

Table 9. Training and implementation details for ImageNet-1K classification, MS-COCO object detection, and ADE20K semantic segmentation. Unspecified hyperparameters follow the respective framework defaults.

Hyperparameter	ImageNet-1K	COCO (det.)	ADE20K (seg.)
Framework	—	MMDetection [3]	MMSegmentation [4]
Head	GAP + MLP	Mask R-CNN [11] + FPN [24]	UperNet [42]
Optimiser	AdamW	AdamW	AdamW
Learning rate	4×10^{-3}	1×10^{-4}	6×10^{-5}
LR schedule	Cosine annealing	MultiStep ($\times 0.1$ at ep. 8,11 / ep. 27,33)	Poly (power 1.0)
Warmup	5% linear	Linear (1k iters)	Linear (1.5k iters)
Weight decay	0.05	0.05	0.05
Batch size	4096	16	16
Duration	300 epochs	$1 \times / 3 \times$ schedule	160k iterations
Input resolution	224×224	1333×800	512×512 crop
Precision	bfloat16	fp32	fp32
EMA decay	0.999	—	—
FPN normalisation	—	Group Norm [41]	—
Augmentation	RandAug [5], flip, crop, jitter, erasing [50], Mixup/CutMix [47,46], LS	Flip ($1 \times$) Flip + LSJ [2] ($3 \times$)	Flip, resized crop ($(0.5, 2.0)$), photometric distortion

B Scan Operator Comparison

We benchmark nine token-mixing operators across spatial resolutions from 32^2 (1K tokens) to 2048^2 (4M tokens). The comparison includes Flash Attention (quadratic, non-causal), Mamba 1D (unidirectional 1D SSM), Vision Mamba (Vim, bidirectional), VMamba SS2D (four independent parallel 1D scans), LocalMamba (window-local 4-direction scan), V2M (two-stage factored four-direction), VSSD (NC-SSD, non-causal), and 2DVMamba (cascaded row-then-column scan). All operators are benchmarked on an NVIDIA RTX 5090 in bfloat16 with batch size 1 and 8 stacked blocks (to reflect realistic activation memory pressure across a model stage), varying only the spatial resolution. Results are shown in Figure 3 and reproduced here in Figure 5 for convenience.

Flash Attention’s quadratic complexity is immediately apparent: each $2 \times$ increase in width and height (i.e. $4 \times$ the number of tokens) multiplies latency by roughly $16 \times$ (consistent with $O(N^2)$), becoming intractable beyond 1024^2 . M2D, by contrast, scales sub-linearly in latency because the wavefront depth

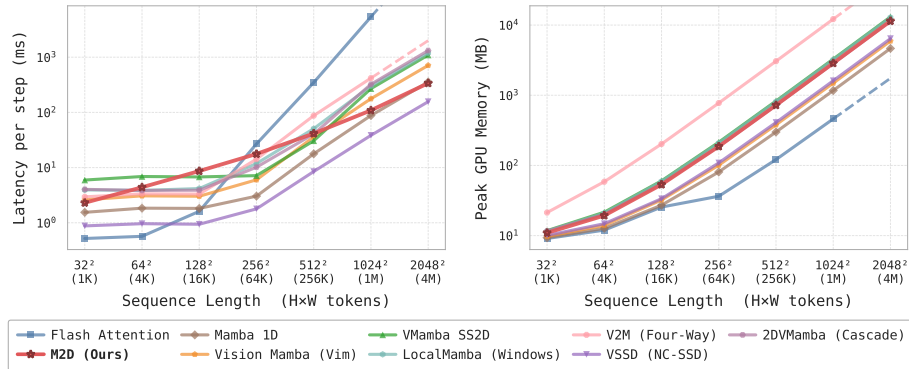


Fig. 5. Kernel-level scaling of nine token-mixing operators across spatial resolutions (32^2 – 2048^2). *Left:* forward-pass latency (ms, log scale). *Right:* peak GPU memory (MB, log scale). Dashed lines denote log-log extrapolations: Flash Attention [7] is capped at 1024^2 due to intractable runtime; V2M runs out of memory at 2048^2 .

grows as $O(\sqrt{N})$, yielding an empirical exponent of approximately $O(N^{0.56})$. This gap widens with resolution: at 1024^2 M2D is roughly $50\times$ faster than Flash Attention, and about $2.5\times$ faster than VMamba SS2D and $4\times$ faster than V2M, both of which pay for multiple independent parallel scans. Although Mamba 1D is modestly faster at low resolutions, the latency gap closes toward 2048^2 as M2D’s sub-linear scaling reduces the deficit. V2M runs out of memory at 2048^2 . The remaining multi-direction operators (VMamba SS2D, LocalMamba, 2DVMamba) maintain similarly linear scaling but at a consistently higher latency offset, reflecting the cost of their multiple independent scan passes.

In terms of peak memory, all SSM-based operators scale linearly. M2D requires roughly $2.5\times$ more memory than Mamba 1D at high resolution, due to its 2D hidden state, and sits at a similar level to VMamba SS2D. V2M requires roughly $4\times$ more memory than M2D, consistent with its out-of-memory failure at 2048^2 . Together, these results confirm that M2D’s wavefront formulation achieves strictly better asymptotic latency than any multi-directional 1D scan decomposition, at a modest and bounded memory overhead over a single 1D scan.

C Kernel Fusion and Recomputation for Memory-Bound SSM Operations

As discussed in the main paper, our wavefront scan operator is memory-bound: the dominant cost is transferring large intermediate tensors through GPU memory, not arithmetic. This mirrors the 1D selective scan in Mamba [12], and makes activation recomputation particularly effective. Recomputing tensors is arithmetically cheap, yet avoids the expensive memory traffic of materialising and reloading them between passes.

We benchmark four strategies for kernel fusion and recomputation as detailed below. Each uses a 16-layer stack of isolated scan operators. This configuration is chosen to reflect the cumulative activation storage across a full model stage. The spatial resolutions tested correspond approximately to the feature map sizes produced by the convolutional stem and subsequent downsampling stages, for inputs from 128^2 to 768^2 : 32×32 , 64×64 , 128×128 , and 192×192 . All results in Table 10 are reported relative to the Naive baseline; the relative savings are consistent across all tested resolutions.

Sequential (reference). A pure Python implementation, iterating over spatial positions in anti-diagonal order using standard PyTorch autograd, with no custom CUDA kernel. Included solely as a correctness reference; it is three orders of magnitude slower than the CUDA baseline and consumes almost double the memory, as PyTorch retains the full autograd computation graph.

Naive. The CUDA baseline with no recomputation. The backward pass requires three tensors of shape $(B \times H \times W \times E_d \times N)$ to remain resident on the GPU between the forward and backward passes, where B is the batch size, $H \times W$ the spatial extent, E_d the channel dimension, and N the SSM state dimension. These tensors are the hidden state sequence \mathbf{h} , and the discretized gate tensors $\bar{\mathbf{A}}_{t,z} = \exp(\Delta \cdot A)$ and $\bar{\mathbf{B}}_{t,z} = \Delta \cdot \mathbf{B} \cdot x$ which constitute the dominant memory cost at all spatial resolutions.

Partial recomputation. The hidden state sequence \mathbf{h} is discarded after the forward pass and recomputed by re-executing the forward kernel at the start of the backward pass. The discretized tensors $\bar{\mathbf{A}}_{t,z}$ and $\bar{\mathbf{B}}_{t,z}$ are similarly never stored as persistent activations. Instead, the backward kernel recomputes $\exp(\Delta \cdot A)$ on-the-fly in registers, retaining only the lower-dimensional continuous-time parameters $(\Delta_t, \Delta_z, \mathbf{B}_t, \mathbf{B}_z) \in \mathbb{R}^{B \times H \times W \times E_d}$ in the saved context. This eliminates all three large tensors from the activation budget.

Full recomputation. Extends the partial strategy by additionally discarding all projected activations after the forward pass, retaining only the raw input x and the learned projection weight matrices. During backpropagation, the input projections are re-executed to reconstruct the projection computation graph, after which \mathbf{h} is recomputed as in the partial strategy. This further reduces the activation footprint at a small additional arithmetic cost.

The Sequential baseline underscores the need for a custom kernel, incurring over $11,000 \times$ the forward wall time and $\sim 180\%$ the peak VRAM of the CUDA baseline. Among the CUDA strategies, recomputation is (as predicted by the memory-bound characterisation) faster end-to-end, not merely more memory-efficient. Partial recomputation reduces peak VRAM to $\sim 19\%$ of Naive while also reducing forward+backward wall time by $\sim 37\%$ and forward-only wall time by $\sim 54\%$. The forward speedup arises because omitting the write of \mathbf{h} and the discretised gate tensors to global memory is cheaper than materialising them, even without a backward pass. Full recomputation reduces peak VRAM further

Table 10. Peak VRAM, forward-only wall time, and forward+backward wall time relative to the Naive baseline for wavefront scan recomputation strategies. Benchmarked using a 16-layer operator stack at 64×64 spatial resolution on an RTX 5090; relative figures are consistent across spatial resolutions from 32×32 to 128×128 . Sequential[†] is a correctness reference implemented in Python with no custom CUDA kernel.

Strategy	Peak VRAM (%)	VRAM Saved (%)	Fwd Time (%)	Fwd+Bwd Time (%)
Sequential [†]	180	—	$\sim 9.7\times 10^3$	$\sim 1.1\times 10^6$
Naive	100	—	100	100
Partial recomp.	19	81	46	63
Full recomp.	10	90	48	65

to $\sim 10\%$ of Naive at a marginal $\sim 2\%$ Fwd+Bwd overhead relative to Partial, making it the preferred strategy when VRAM is the primary constraint.

At 192×192 spatial resolution (corresponding to a 768×768 input at $4\times$ stride), the Naive baseline exceeds the 32 GB memory budget. As PyTorch allocates the full `ctx` tensors (\mathbf{h} , $\overline{\mathbf{A}}_{t,z}$, $\overline{\mathbf{B}}_{t,z}$) during the forward phase in anticipation of a potential backward, the Naive variants without recomputation cannot even run inference (forward-only) at this resolution on a 32 GB GPU. Both recomputation variants remain well within budget at 192×192 . Recomputation is therefore not merely a training optimisation but a prerequisite for high-resolution inference in downstream tasks.